

Development of a Fourier Technique for Automated Spiral Galaxy Classification

A. R. Butler

Calvin College, Grand Rapids, MI 49546

arb6@calvin.edu

ABSTRACT

Galaxy classification has historically been a matter of visually inspecting galaxy images and categorizing them according to their appearance. Recently, however, more efficient and quantitatively meaningful classification methods have been required for analysis of galaxy formation and evolution from the ever-growing amount of data available to the astronomical community. We present an automated method of reconstructing select galaxy images from the Ohio State University Bright Spiral Galaxy Survey using two-dimensional Fourier models of galaxies. Fourier series are fit to azimuthal profiles of concentric annuli centered on each galaxy. Particular harmonics in the Fourier series for each annulus are analyzed to recognize bars and spiral arms and to quantify their strength. One barred spiral galaxy and one non-barred spiral galaxy are used to illustrate the technique and to come to some preliminary conclusions.

Subject headings: galaxies: fundamental parameters (classification, surface brightnesses) — galaxies: general — galaxies: photometry — galaxies: surveys — galaxies: spiral — galaxies: structure

1. Introduction

Morphological classification of galaxies is a crucial foundation for the understanding of the physical dynamics of galaxies (de la Calleja & Fuentes 2004). Even though morphological classification is not physical classification, it is an indispensable guide to asking relevant questions about the physics associated with structures in galaxies (Es-kridge et al. 2002). Buta et al. (1994) showed that mean galaxy types classified by experienced human classifiers can be correlated with global properties such as color, hydrogen index, and mean effective surface brightness. Quantities like these are related to major physical properties like stellar populations, star formation rate, stellar surface density, and total mass of the galaxy (Ode-wahn et al. 2002). Thus, measurable parameters extracted from the structure a galaxy can be translated into meaningful physical properties of that galaxy.

Historically, galaxy classification has been a matter of visually inspecting two-dimensional im-

ages of galaxies and categorizing them as they appear. Even though human classification by expert classifiers is somewhat reliable, it is simply too time-consuming for the extremely large amounts of astronomical data taken in recent years. Not only this, but experience and skill, traits that only expert classifiers possess, are required (Naim et al. 1995). Hence, it is crucial to develop an automated, objective, and quantitatively descriptive method of galaxy classification in order to efficiently characterize the vast amounts of data that have been taken and to more accurately relate the results of these automated methods to physical properties of galaxies.

Many different methods have been developed for this very purpose. Artificial neural networks (ANNs), originally created to simulate groups of neurons and their ability to learn, have been discovered to have many practical applications for automated galaxy morphology. For example, Storrie-Lombardi et al. (1992) used an ANN to classify galaxies based on back-propagation using 13 input photometric parameters from the ESO-

LV catalog. With their five classes (E, S0, Sa+Sb, Sc+Sd, and Irr), their method succeeded 64% of the time when the most probable output represented the class and 90% of the time when the highest or second highest probable output represented the class. Odewahn et al. (2002) developed another method that employed Fourier models to reconstruct galaxy images, fitting Fourier series to the azimuthal profiles of concentric annuli centered on the galaxies. They used artificial neural networks to train classifiers that could identify bar features at the 80-90% confidence level and correctly output the Hubble type with a 1.0σ scatter of 1.5 steps on the stage axis of the revised Hubble system.

In this paper, the Fourier technique presented in Odewahn et al. (2002) is used to reconstruct the images of one barred spiral galaxy and one non-barred spiral galaxy for which the method worked well. In §2, we describe the data we used. Sections §3 – §11.3 describe the actions taken to calibrate each image and to set them up for Fourier reconstruction. The Fourier method and analysis are described in detail in §12 and §13. Lastly, §14 summarizes our results and makes suggestions for future work. Although we did not use any ANNs, we plan on including the output from this work in a much larger data set to be used as input for an ANN.

2. Data

We used 189 B-band images of bright (~ 26 mag/arcsec² $\leq \mu_B \leq \sim 20$ mag/arcsec²) spiral galaxies taken by Ohio State University (OSU) for its Bright Spiral Galaxy Survey (Eskridge et al. 2002). See OSU’s website¹ for information on targets and instruments used as well as image parameters.

3. Building the CCD Image Library

We compiled a library of the B-band images with the AIMTOOL package in LMORPHO². The library contained files that stored information for each image, such as file path, number tag, celestial coordinates, exposure time, and filter.

¹<http://www.astronomy.ohio-state.edu/~survey/EDR/Data/>

²Constructed by Steve Odewahn (University of Texas at Austin).

4. Sky-Mapping

Subtracting the sky in an image of a galaxy is very important for performing surface photometry. In the B-band, the surface brightness of the outer regions of a typical nearby galaxy is fainter than that of the night sky by about 5 mag/arcsec², which corresponds to a factor of 100 in flux. Thus, extreme care must be taken to precisely compute the sky surface brightness and to subtract it from the image so that only the signal from the galaxy remains. An imprecise sky value can lead to an uncertain calculation of the photometric zero point (see §10.1), which can result in an uncertain surface brightness in the standard Johnson photometric system. Thus, this is a crucial step.

We used AIMTOOL’s SKYMAP task to map the sky, setting the object detection threshold to 2.0σ above the average sky level. This made it so that any pixel that had a value 2.0σ above the average sky level was not mapped as part of the sky. Many images contained a substantial amount of bad pixels, so this preliminary sky mapping step was not sufficient for those images. For a description of the method we used to accurately map the sky for these bad images, see §8. Unfortunately, we have not reached the point where we can determine the precision of all our sky values. However, the sky values we initially calculated were good enough for preliminary analysis (see §9 and §11.2).

5. Rebuilding the CCD Image Library

Once we calculated the sky statistics, we wanted that information written in the library. So, we deleted all the files in the directory in which we ran AIMTOOL, and re-ran it to compile the updated information for each image. In addition, we used AIMTOOL to identify all image sets of the same galaxy to within a certain positional tolerance, which we specified as 120 arcseconds. All images that had the same right ascension (RA) and declination center on the sky were found within this tolerance. This created a file that contained the number of unique positions there was for each galaxy. In our case, since all of our images were taken in one filter, the number of unique positions equaled the number of images.

6. Cross-matching to the RC3 Catalog of Galaxies

6.1. Building an RC3 Catalog

Next, we used LMORPHO’s RC3TOOL package to create files that contained names and J2000 coordinates of galaxies in the RC3 (Third Reference Catalog of Bright Galaxies). This was useful because AIMTOOL would use these files in the next step (§6.2) to identify RC3 galaxies in the image library and attach a PGC (Principal Galaxy Catalog) number to that galaxy. A later step (§7) would require the PGC numbers of the galaxies to quickly find aperture photometry for each galaxy.

6.2. Finding RC3 Galaxies in the Library

Naturally, the next step was to cross-match the images in the library to the RC3 catalog, associate PGC numbers with them, and update the information files in the library with the results. We used AIMTOOL’s UPDATE task for this action. If an image didn’t match with the RC3 catalog using a name, UPDATE searched for it positionally. We specified a 180 arcsecond positional tolerance in case there were large uncertainties in the right ascension and declination in the image headers. To review, this operation found galaxies in the RC3 catalog and attached PGC numbers to those galaxies, which is important for the next step.

7. Gathering Aperture Photometry for the Library

We used AIMTOOL’s APDATI task to gather any available aperture photometry (which was sky-subtracted when it was measured) for each galaxy. APDATI searched for the galaxies in the library by their PGC numbers and retrieved the data for those galaxies in a previously compiled database. The aperture photometry would become more significant later when we calculated the photometric zero point (see §10.1).

8. Locating the Galaxies

Of course, in order to actually perform galaxy surface photometry, the galaxy must be accurately located in each image. We used AIMTOOL’s XPADISPLAY task to view each image with ds9 and mark the shape and location of each galaxy

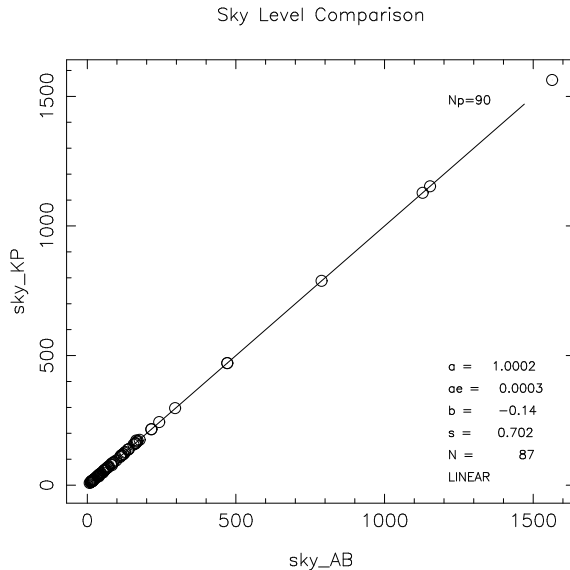


Fig. 1.— Comparison of sky results for the author and another human classifier.

with an ellipse region. The ellipse parameters (length of the semi-major axis, b/a , pixel position of the center, and position angle) were subsequently recorded for each image in the library. Also, for “bad” images (ones that had an excess of bad pixels), we manually specified pixels that covered the sky with box regions to ensure that AIMTOOL wouldn’t count artifacts in the images as the sky.

9. Re-mapping the Sky

Now that the sky areas had been specified for “bad” images, the sky was re-mapped for these images. In general, the computed sky values were negligibly different, but the standard deviations were significantly lower than those obtained by the automatic sky mapping routine. Thus, we succeeded in obtaining more precise sky values using this manual technique, which is what we needed. In fact, another human classifier performed the same sky mapping step, and even though he mapped slightly different sky regions for the images that required manual sky mapping, all of our sky values were almost exactly the same (see Fig. 1). This ensured that our sky values were repeatable and independent of exactly how one mapped the sky. However, this didn’t mean

that we had obtained precise sky values – the possible systematic error introduced by the bad pixels in some of the OSU images needs to be investigated in future work. See §11.2 for justification of the ignorance of the precision of our sky values.

10. Preparing the Galaxies for Surface Photometry

10.1. Computing the Photometric Zero Point

Now that the sky had been determined in a repeatable fashion, the zero points could be computed using AIMTOOL’s ZPAPRUN. For each image, the routine subtracted the sky and used the ellipse parameters specified in §8 to locate the center of each galaxy. The total fluxes inside circular apertures that were the same sizes as the various circular apertures gathered in §7 were calculated. The Pogson equation,

$$m_B = ZP - 2.5 \log f, \quad (1)$$

was used to compute the zero point for a given aperture. Here, m_B is the integrated B-band magnitude in the standard Johnson photometric system for a given aperture, f is the measured integrated flux inside that aperture, and ZP is the zero point. For a given aperture, the magnitude from the aperture photometry in the catalog differed from the measured magnitude (just how much they differed depended on the image quality and the accuracy of the sky value). Since there were multiple apertures for each galaxy, there were multiple zero point values to choose from. Thus, a systematic way of arriving at the zero point for each image went as follows:

1. The zero points calculated according to Eq. 1 for each aperture were plotted versus the corresponding aperture areas.
2. Using ZPARUN’s interactive PGPLOT¹ routine, we rejected outlying points.
3. The zero point and its error were computed using the average and standard deviation of the remaining points, respectively, and stored in a file that contained the zero points for each image.

¹Created by Tim Pearson (California Institute of Technology).

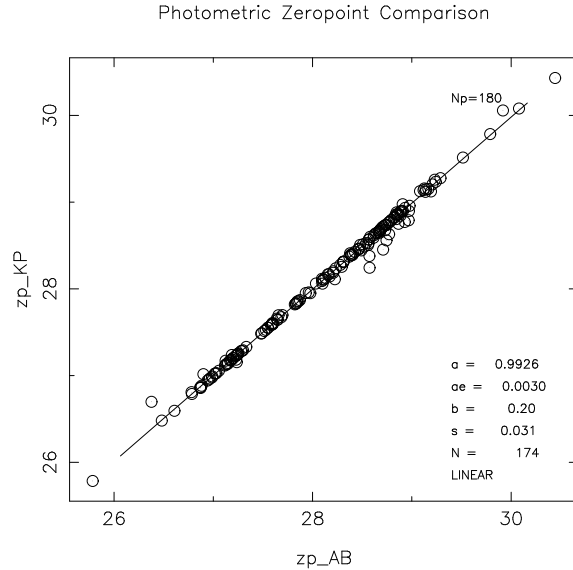


Fig. 2.— Comparison of zero point results for the author and another human classifier.

As for the sky, another human classifier (the same one as in §9) computed the zero points independently. Fig. 2 shows that our values were very nearly the same for each image. For all practical purposes, this indicated that we could use these zero points without introducing any significant bias in the analysis.

10.2. Rebuilding the Library - Second Pass

To update the CCD image library with this information as well as the new sky statistics calculated in §9, we deleted all the files in the directory in which we ran AIMTOOL, and re-ran AIMTOOL to compile the fresh information for each image. We now could compute the surface brightness for each galaxy in terms of the standard Johnson photometric system using the following equation:

$$\mu_B = ZP - 2.5 \log \left(\frac{f}{A_{pix}} \right) \quad (2)$$

Once we measured the flux per unit area (f/A_{pix}) of the ellipse in the image, we could simply plug that number and the zero point into Eq. 2 to compute the surface brightness (μ_B).

11. Galaxy Surface Brightness Profiles

11.1. Initial Construction

Surface brightness profiles were created for the purpose of quantifying how repeatable the flux measurements were. Another human classifier (the same one as in §9 and §10.1) performed the exact same actions taken in §3 - §11.1. The results are compared in §11.2.

We used LMORPHO’s IGALPHOT package to compute an elliptically averaged surface brightness profile for each galaxy. IGALPHOT used the ellipse parameters, sky statistics, and zero points determined in §8, §9, and §10.1, respectively, to subtract the sky and properly calculate the flux. We divided each galaxy into 30 annuli with a width that depended on the semi-major axis of the ellipse specified in §8. The longer the semi-major axis, the wider the annuli. The annuli extended out to some radius greater than that of the semi-major axis of the ellipse. The elliptical average of the surface brightness was computed for each of the 30 annuli and plotted versus the semi-major axis of each corresponding ellipse.

11.2. Confirming the Results

Upon comparison of each of our surface brightness profiles, shown in Fig. 3, we found that the scatter increased with fainter surface brightnesses. At the bright end ($\mu_B \sim 22$ mag/arcsec²), there was a scatter of 0.14 mag/arcsec². At the faint end, the scatter was 0.40 mag/arcsec². This was exactly what we expected because of the lower signal to noise ratio at dimmer surface brightnesses. Most importantly, the systematic error in the mean residuals did not exceed 0.2 mag/arcsec². These results indicated that not only were our surface brightness calculations reasonably accurate, but our sky values and zero points were also being computed in a systematically consistent way. This ensured us that our methodology was fundamentally reliable.

11.3. Star Removal

To be sure, there were many images in which stars overlapped the target galaxy. These stars showed up in the surface brightness profiles as large spikes. See NGC 488’s profile in Fig. 4 for an example. In §12, the stars are patched out us-

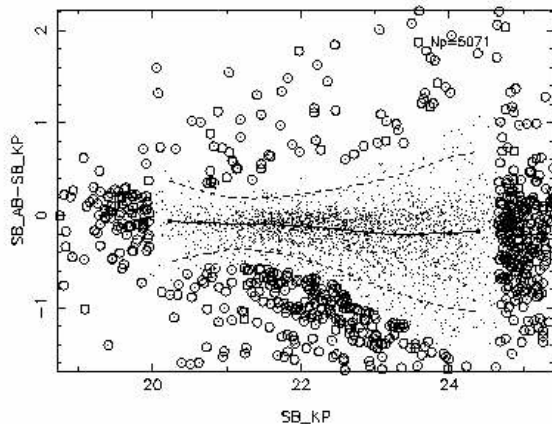


Fig. 3.— Comparison between surface brightnesses for the author and another human classifier (residuals vs. surface brightness results for the other human classifier). The solid line is the fit for the mean residuals and the dashed lines are the 2σ loci.

ing IGALPHOT, and in Fig. 5, NGC 488’s surface brightness profile is shown again with the stars removed.

12. Fourier Analysis

Now we were ready to perform two-dimensional Fourier analysis on the galaxy images. IGALPHOT was used to execute the method. It used the ellipse parameters, sky statistics, and zero points determined in §8, §9, and §10.1, respectively, for the same reason as in §11.1. Each galaxy image was divided into a certain number of annuli that had the same shape as the initial ellipse used to describe the location and shape of the galaxy, as described in §8. See Table 1 for the semi-major axis length (a) of this ellipse for each galaxy and the number of annuli chosen. We attempted to roughly maintain the relative widths of each annulus for each galaxy.

Before the actual Fourier analysis was done, the stars were patched out using IGALPHOT’s built-in star removal algorithm. The stars were essentially very high spatial frequency objects, so it was difficult for IGALPHOT to fit a Fourier series to annuli that contained stars. Hence, it was essential that the stars be removed so that the true

NGC 488

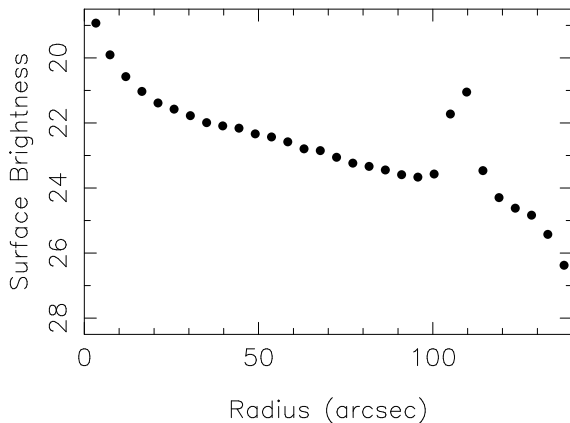


Fig. 4.— Initial surface brightness profile of NGC 488. The bump at 110 arcseconds is a star situated between the core and outer regions of the galaxy. (The units of surface brightness were mag/arcsec²).

NGC 488 Patched

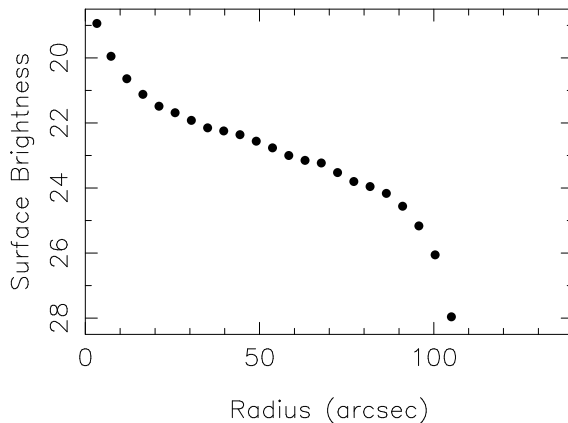


Fig. 5.— Surface brightness profile of NGC 488 with the stars patched out. The star at the outer edges of the galaxy was removed, so the surface brightness dropped much more sharply than it did in Fig. 4. (The units of surface brightness were mag/arcsec²).

Galaxy	a (")	No. of Annuli	" /annulus
NGC 4314	140	80	1.75
NGC 5427	80	45	1.78

Table 1: Length of semi-major axis of ellipse used to describe location and shape of each galaxy and the corresponding number of annuli used for the Fourier models.

structure of each galaxy could be modeled as accurately as possible. Once the stars were removed, IGALPHOT integrated the surface brightness for a given azimuthal angle over the width of a given annulus, and assigned that intensity value to that angle. It repeated that process for each angle in the annulus and for all annuli. It then plotted intensity versus azimuthal angle for all annuli, starting from the semi-major axis, and fit a Fourier series to each profile. At most, it used the first 16 harmonics of the Fourier series to fit the data according to the following equation:

$$I_0(r, \theta) = I_0 + \sum_{m=1}^{16} (a_m \cos m\theta + b_m \sin m\theta) \quad (3)$$

The I_0 term represents the average intensity of the given azimuthal profile, so it is a constant term. The a_m and b_m terms are simply the coefficients of

the cosine and sine terms, respectively, for a given integer value of m . They're given by:

$$a_m = 2\langle I(r, \theta) \cos m\theta \rangle \quad (4)$$

$$b_m = 2\langle I(r, \theta) \sin m\theta \rangle \quad (5)$$

Finally, θ represents the angle subtended from the semi-major axis of the galaxy in its equatorial plane. These are the same variables and formulae used in Odewahn et al. (2002).

One clearly barred spiral galaxy and one clearly non-barred spiral galaxy from the OSU Bright Spiral Galaxy Survey were chosen, based on their good results from the Fourier analysis, to be analyzed in parameter space. They are described in detail below. The annulus shown for each galaxy was the one that gave the best Fourier fit. The results for the two galaxies are compared in §13 and used to distinguish between the different features in each galaxy and to quantify their strength.

NGC 4314.—SB(rs)a: Has a well-defined bulge and bar, which are very bright compared to the spiral arms. Fig. 6 shows the Fourier series fit for annulus 25, which is in excellent agreement with the data. The two high-intensity, conspicuous fea-

tures are from the prominent bar going through the center of the galaxy.

NGC 5427.—SA(s)c: Grand design spiral with a large, prominent core. The arms are slightly distorted due to the galaxy’s interaction with its nearby companion, NGC 5426. See Fig. 7 for the Fourier model fit for annulus 10. Even though IGALPHOT didn’t fit the data as well as it did for NGC 4314, it still fit the overall structure very well.

13. Parameter Space Analysis

Once the Fourier data for the two galaxies was obtained, the galaxies could be analyzed in parameter space. The trends we expected to see in the data were in the 2θ amplitude and phase angle (the angular position of the peak of the 2θ harmonic) and the 16θ amplitude. The amplitude of a given harmonic in the Fourier series is a measure of the relative contribution of that harmonic. For a given annulus, the expression for the amplitude of a given harmonic is

$$A_m = \sqrt{a_m^2 + b_m^2}/I_0 \quad (6)$$

Again, this is the same equation used in Odewahn et al. (2002).

First, we analyzed the 2θ amplitude as a function of annulus number for each galaxy. Fig. 8 shows that NGC 4314’s 2θ amplitude peaked at a value of about 0.8. On the other hand, NGC 5427’s amplitude peaked at about 0.4 (see Fig. 9). This is because NGC 4314’s bar was almost perfectly symmetric, which translated to the two well-defined humps in the azimuthal profiles (see Fig. 6). Thus, the 2θ harmonic was the one that contributed the most to fitting the profile. On the other hand, NGC 5427’s spiral arms were not nearly as symmetric or simple as the bar in NGC 4314, so the Fourier series fits required less of a contribution from the 2θ harmonic and more of a contribution from other harmonics.

Upon examining the plots of the 2θ phase versus annulus number for each galaxy, we noticed a difference between bars and spiral arms. The bar in NGC 4314 was contained between annulus 20 and annulus 40. Fig. 10 shows that in between those two annuli, the phase angle stayed constant to within a few degrees. This was to be expected, since the position angle of the bar did not change

relative to the semi-major axis of the galaxy. NGC 5427 also met our expectations. In Fig. 11, the 2θ phase for that galaxy is seen to change significantly in between annulus 10 and annulus 20. This was due to the rapidly changing position angle of the spiral arms in that region relative to the semi-major axis of the galaxy. In fact, the 2θ position angle changed by almost 180° , which is approximately the same amount by which the position angle of the spiral arms changed in between these two annuli. The signature of the changing position angle of the spiral arms was also evident for NGC 4314 (see Fig. 10). Outside the region of the bar (past annulus 40), the 2θ phase changed by about 90° , which is about the same amount by which the position angle of the spiral arms changed.

Lastly, we investigated the contribution of the 16θ term to the Fourier models of each galaxy. We did this to see what kind of structures required the highest order term to be correctly modeled. In Fig. 12, the 16θ amplitude as a function of annulus number for NGC 4314 is shown. As can be seen, the 16θ amplitude systematically peaked at around 0.06 at about annulus 30. This was almost exactly where the galaxy’s 2θ amplitude peaked (see Fig. 8). Furthermore, the 16θ amplitude was slightly less than 10% of the 2θ amplitude at that annulus. These observations indicate that the 16θ term was a significant contributor to the overall Fourier fit of the bar. By contrast, NGC 5427’s 16θ amplitude peaked at a location well outside the spiral arms, in the vicinity of annulus 30 (see Fig. 13). Upon investigation, we found that annulus 30 overlapped two bright HII regions. The azimuthal profile for this annulus (Fig. 14) clearly shows that IGALPHOT had difficulty in fitting the data, especially the sharp peaks caused by the HII regions. This implies that extremely high order Fourier terms were needed to fit the sharp, knotted structure in the spiral arms.

Perhaps all of these observations are a general trend, but a much larger sample of galaxies is needed in order to come to any meaningful conclusions.

14. Conclusion

So far, we have constructed a simple paradigm for structure recognition in nearby galaxies. In summary, the peak value of the 2θ amplitude

seemed to be a good indicator of whether or not a galaxy had a prominent bar. The larger 2θ amplitude peak belonged to NGC 4314, a strongly barred spiral galaxy, and the smaller 2θ amplitude peak belonged to NGC 5427, a non-barred spiral galaxy. We interpreted this result as being caused by the asymmetry and less orderly structure of the spiral arms in NGC 5427. Moreover, the 2θ phase angle recorded how the position angle of the major features in the galaxies changed. The bar in NGC 4314 was a feature whose position angle relative to the semi-major axis of the galaxy did not change, so its 2θ phase did not change over the range of annuli in the region of the bar. NGC 5427's 2θ phase did change over the range of annuli in the region of the spiral arms, so this signified that the spiral arms themselves were changing their position angle with radius. Lastly, the 16θ amplitude suggested what kinds of structures in the galaxies were of high spatial frequency. For the barred galaxy NGC 4314, the 16θ term was needed to fit the steep bar. For the non-barred galaxy NGC 5427, the 16θ term was needed to fit all the sharp, discrete features like the HII regions in the spiral arms, even though it was clear that more terms were needed to better fit the profile.

These observations need to be confirmed in a later work, but for now, this method works best with barred-spiral galaxies with well-defined, bright bars. As mentioned in §13, these are simply preliminary conclusions arrived at by examining two galaxies in detail. Future work on this method must include these galaxies in a much larger data set, the results of which will hopefully be used as input for an ANN (as described in §1) or possibly a decision tree. Before we do that, however, we need to spatially filter the azimuthal profiles of the galaxies with a stellar PSF so that the HII regions and other features of high spatial frequency can be smoothed out. That way, there would be no need to add an absurd amount of terms to fully model the spiral arms, especially of later type galaxies, which have more HII regions than other types.

In addition, this method could be developed further to work in higher redshift environments. In fact, Abraham et al. (1994) has already developed a method for morphologically classifying galaxies up to $z \sim 0.5$ based on direct measurement of central light concentrations of galaxies. Their method is less sensitive to seeing degradation than the

Fourier technique used in this paper (see Odewahn et al. (2002) for an in-depth explanation of how the resolution and signal to noise ratio can drastically change the success rate of bar detection). Perhaps methods like the one presented in this paper and that of Abraham et al. (1994) could be combined for preparation of an automated method to classify galaxies in deep images. By determining the number of and types of barred galaxies in the high redshift universe, this kind of a method could accelerate our understanding of galaxy formation and evolution.

I want to thank Dr. Stephen Odewahn for his extensive knowledge on galaxy surface photometry and Fourier analysis as well as his helpful guidance during this project. I am also grateful to Dr. Matthew Shetrone, who applied to the NSF for the funding of McDonald Observatory's summer REU program. Additionally, I thank Kyle Penner for repeating my measurements as described in §11.1. Lastly, I thank the NSF itself for providing the grant that supported my research.

This work made use of data from the Ohio State University Bright Spiral Galaxy Survey, which was funded by grants AST-9217716 and AST-9617006 from the United States National Science Foundation, with additional support from the Ohio State University.

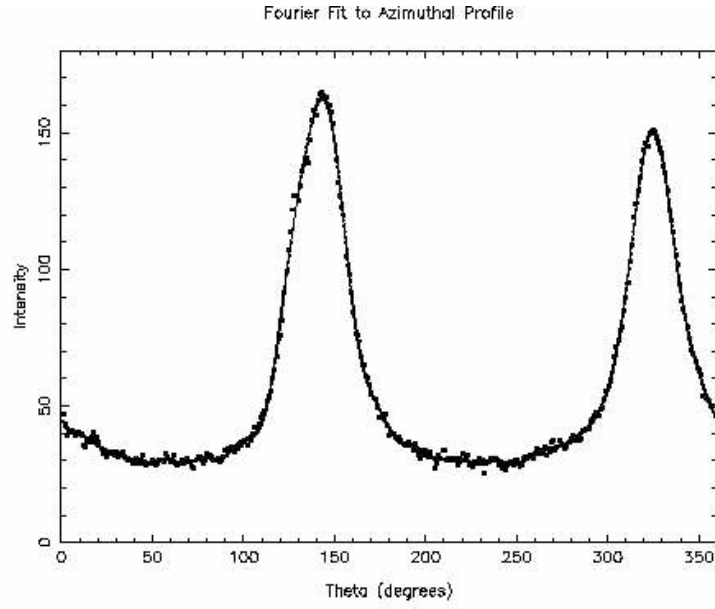


Fig. 6.— Fourier series fit for annulus 25 of the model for NGC 4314.

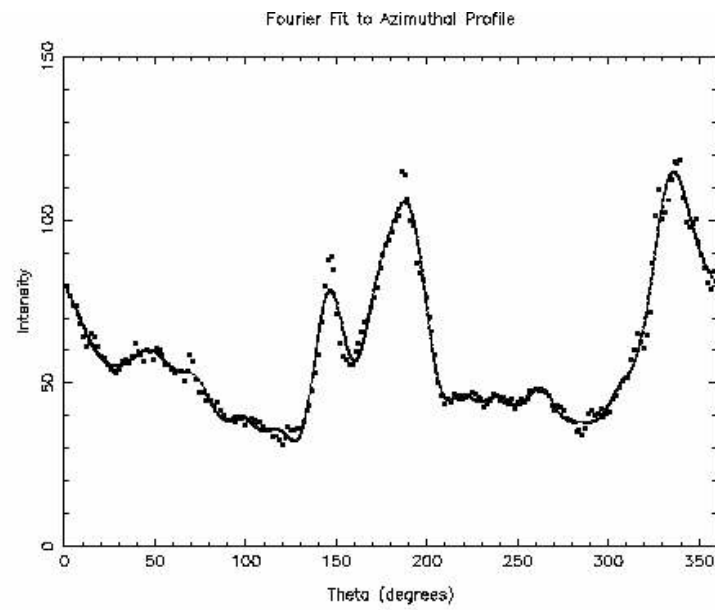


Fig. 7.— Fourier series fit for annulus 10 of the model for NGC 5427.

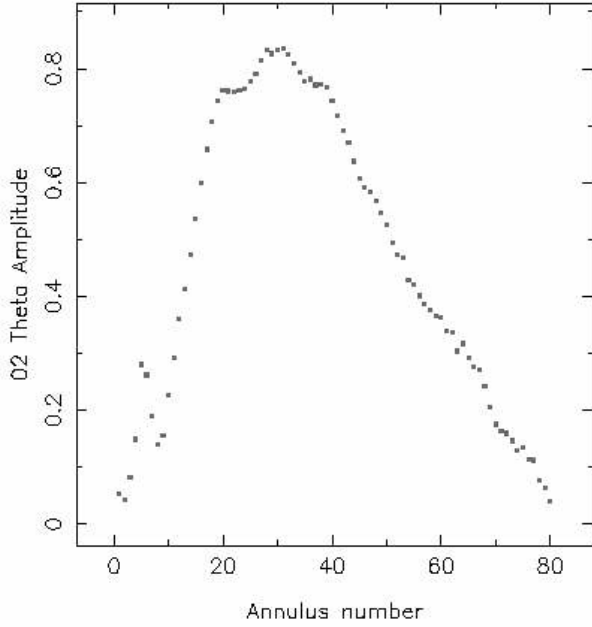


Fig. 8.— 2θ amplitude for each annulus of the Fourier model for NGC 4314.

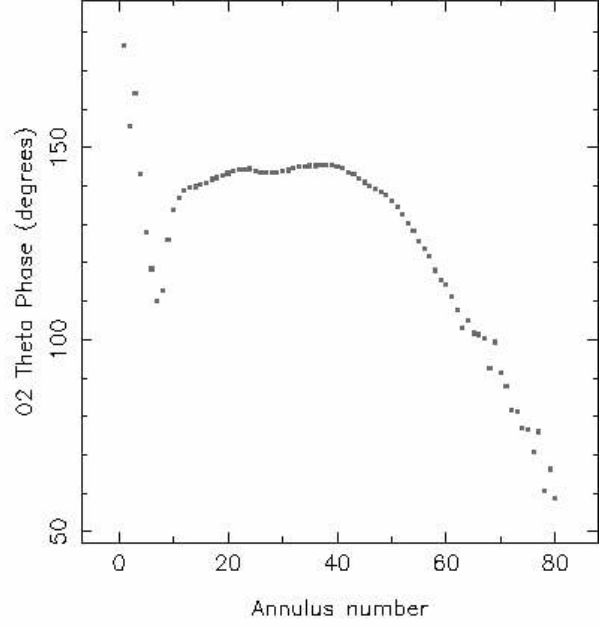


Fig. 10.— 2θ phase for each annulus of the Fourier model for NGC 4314.

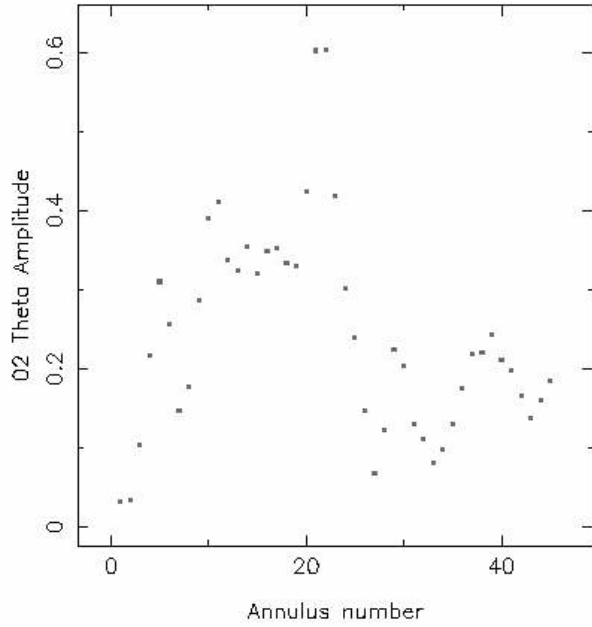


Fig. 9.— 2θ amplitude for each annulus of the Fourier model for NGC 5427.

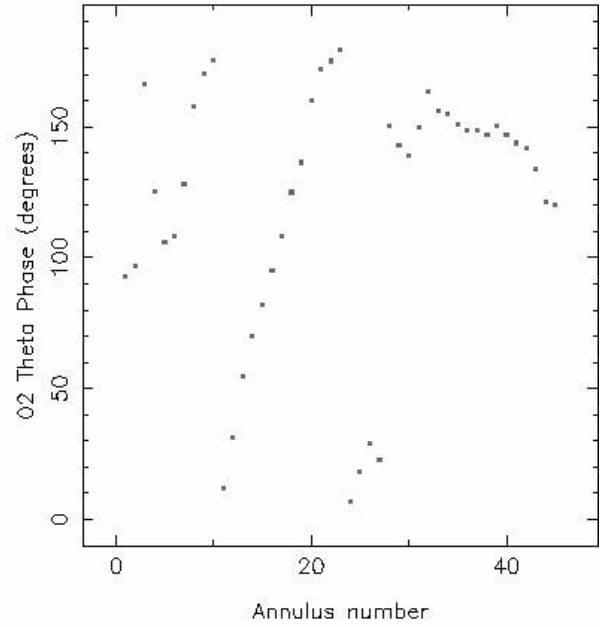


Fig. 11.— 2θ phase for each annulus of the Fourier model for NGC 5427.

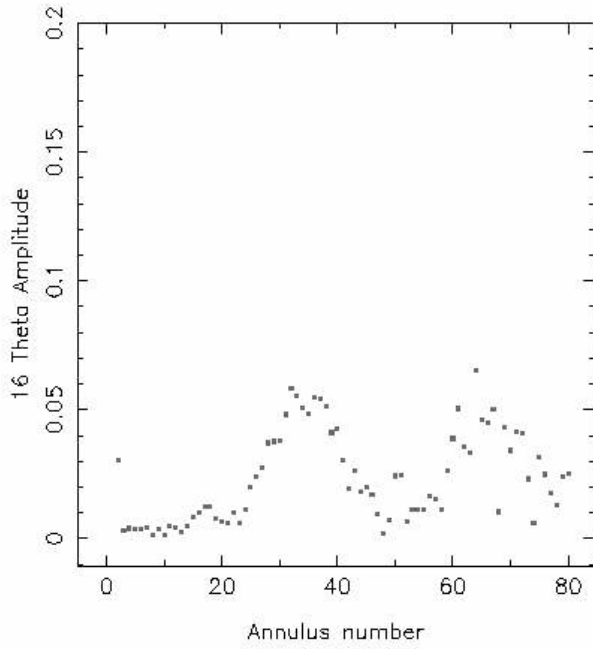


Fig. 12.— 16θ amplitude for each annulus of the Fourier model for NGC 4314.

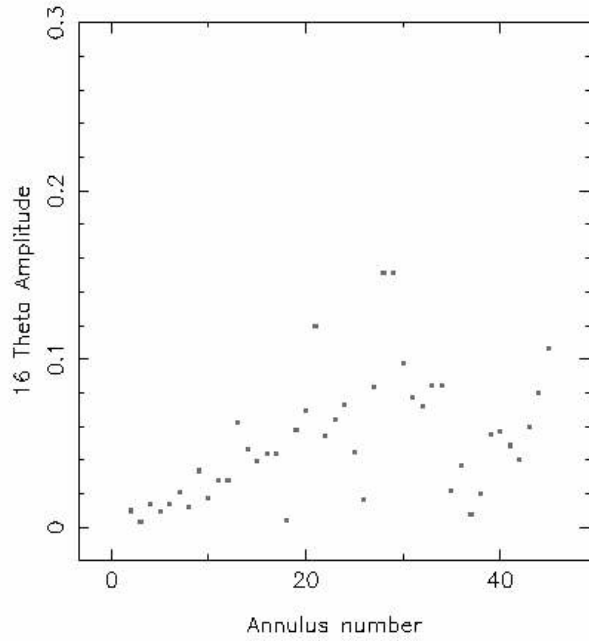


Fig. 13.— 16θ amplitude for each annulus of the Fourier model for NGC 5427.

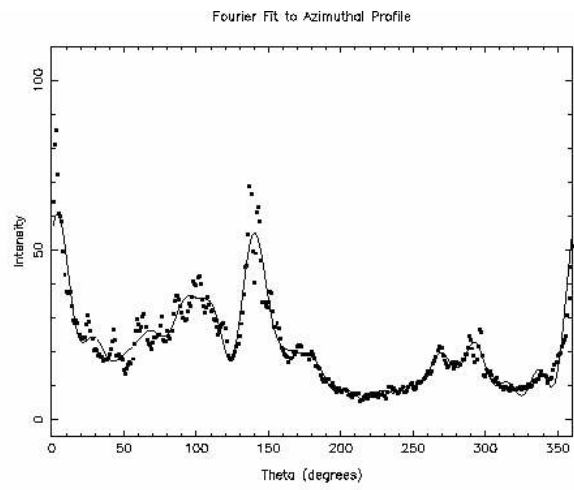


Fig. 14.— Fourier series fit for annulus 30 of the model for NGC 5427.

REFERENCES

- Abraham, R. G., Valdes, F., Yee, H. K. C., & van den Bergh, S. 1994, *ApJ*, 432, 75
- Buta, R., Mitra, S., de Vaucouleurs, G., & Corwin, Jr., H. G. 1994, *AJ*, 107, 118
- de la Calleja, J. & Fuentes, O. 2004, *MNRAS*, 349, 87
- Eskridge, P. B., Frogel, J. A., Pogge, R. W., Quillen, A. C., Berlind, A. A., Davies, R. L., DePoy, D. L., Gilbert, K. M., Houdashelt, M. L., Kuchinski, L. E., Ramírez, S. V., Sellgren, K., Stutz, A., Terndrup, D. M., & Tiede, G. P. 2002, *ApJS*, 143, 73
- Naim, A., Lahav, O., Sodre, Jr., L., & Storrie-Lombardi, M. C. 1995, *MNRAS*, 275, 567
- Odehahn, S. C., Cohen, S. H., Windhorst, R. A., & Philip, N. S. 2002, *ApJ*, 568, 539
- Storrie-Lombardi, M. C., Lahav, O., Sodre, Jr., L., & Storrie-Lombardi, L. J. 1992, *MNRAS*, 259, 8P